Formation of negative ions from fluorine projectiles scattered off a MgO(100) surface: Theory

Stefan A. Deutscher, Andrei G. Borisov, and Victor Sidis
Laboratoire des Collisions Atomiques et Moléculaires (Unité Mixte de Recherche No. 8625), Bâtiment 351, Université de Paris–Sud, 91405 Orsay Cedex, France
(Received 14 December 1998)

We present a parameter-free theoretical study of the negative-ion production from fluorine projectiles during low-energy (0.5–4 keV), small incidence angle (3.5°) collisions with a MgO(100) surface. Our calculations are based on the binary encounter model developed to describe the electron capture by a projectile upon collision with an insulating ionic crystal surface [see A. G. Borisov and V. Sidis, Phys. Rev. B **56**, 10 628 (1997)]. For the low-velocity behavior of the negative-ion yield, good agreement is obtained between our theoretical results and the available experimental data by S. Ustaze *et al.* [Phys. Rev. Lett. **79**, 3526 (1997)].
[S1050-2947(99)09805-4]

PACS number(s): 79.20.Rf, 34.70.+e

I. INTRODUCTION

Following an extended period of in-depth studies on the interaction of atomic and molecular projectiles with metal surfaces [1–4], increased attention has recently been devoted to insulating surfaces of ionic crystal targets [5–23]. A wealth of experimental data for a variety of projectile-target combinations is meanwhile available on charge exchange, electron emission, secondary ion emission, and energy loss [6,9,10,12–16,20,21]. In particular, the evolution of the charge state of a projectile in low-energy, grazing-incidence ($\varphi \simeq 0.5° - 10°$) collisions has been studied by various experimental and theoretical groups [7,10–14,16–19,22,23]. Just as Al surfaces are an excellent metallic prototype target, which behaves as a nearly free electron gas well described by the jellium model [24], ionic crystals such as LiF, KI, and KCl have assumed the same role for the investigation of projectile-insulator systems.

Ionic crystals are characterized by the localization of positive and negative charges at the lattice sites and by high binding energies of the valence electrons. These materials have a large energy gap ($E_g \simeq 6-14$ eV) between conduction and valence bands (see Fig. 1). At $E_{\mathrm{VB}} \lesssim -8$ eV, their upper valence-band (VB) edge lies low compared with the the affinity level of a typical projectile. Their lower conduction-band (CB) edge, on the other hand, is positioned close to the vacuum level ($E_{CB} \gtrsim -2$ eV) in the case of LiF even 2 eV above it [25–31]. Such targets behave as insulators on the time scale of the collision relevant for the charge exchange between projectile and surface (about 10^{-14} s$\simeq$400 a.u.) [22], while at appropriate temperatures (a few hundred degrees Celsius) their *ionic conductivity* is large enough to avoid a charge buildup at the surface during the course of the experiment [5].

In experiments with alkali-halide surfaces, the formation of a very high negative ion fraction from neutral H, O, and F projectiles has been observed [11,13,23] despite the large energy difference between the affinity level of the projectile (-0.754, -1.46, and -3.40 eV, respectively [32]) and the occupied electronic states in the valence band. This at first surprising result was explained by charge transfer via a series of binary encounters of the projectile with the negatively charged lattice ions [17]. In the final state of the electron transfer reaction, the negatively charged projectile interacts with the hole left at the surface by electron capture. This attractive interaction drastically reduces the energy defect of the electron transfer (energy-level confluence), and, therefore, makes possible the formation of negative ions from a neutral projectile (cf. Fig. 1). Once formed, the negative ion has a large probability to survive in front of the surface of the ionic crystal because of the large band gap that suppresses the electron loss.

The high efficiency observed in the negative-ion production is of interest, for instance, for the design of low-flux negative-ion beam sources and in space research for the construction of neutral particle detectors. On a more fundamental level, the majority of chemical reactions on surfaces involve an electron exchange [33]. Hence it is important to understand such charge-transfer phenomena.

Lately, the range of investigated systems has been expanded to include insulating oxide surfaces, which are of technological relevance and have numerous industrial applications in catalysis, glass industry, microelectronics, and ceramics, as prospective materials for fusion reactors, and so on [34]. Measurements with 4-keV H projectiles in grazing collision with a Mg(100) surface were reported [35] that investigated the negative-ion yield as a function of the oxygen coverage of the surface. They showed, after an exposure of only a few Langmuir, a H^- yield of up to 6%, which is a significant increase compared with the yield on a clean Mg surface (about 1%). More recent measurements [36] of 0.5–4-keV fluorine, hydrogen, and neutral oxygen projectiles colliding with a MgO(100) surface under a grazing angle of 3.5° show features similar to those observed for alkali-halide targets: a very large negative ion fraction (up to 70% for fluorine) is registered, indicating the presence of a very efficient electron-capture mechanism. The same experiment gave also evidence for the existence of a non-negligible electron loss channel, leading to the destruction of negative ions.

This paper will present the results of our calculations for the electron capture to the projectile during grazing scattering of fluorine atoms from an MgO(100) surface. It is organized as follows: Sec. II gives a brief review of the theory of the binary encounter model, Sec. III deals with the descrip-

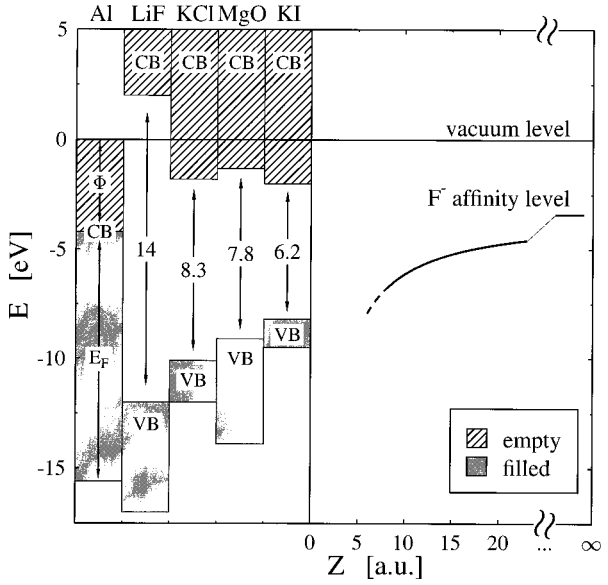

FIG. 1. Sketch of the energetic positions of valence (VB) and conduction (CB) bands of several ionic crystal targets with respect to the distance (Z) dependent energy of the F^- projectile affinity level. E_F and Φ denote the Fermi energy and work function of Al, which is shown for comparison.

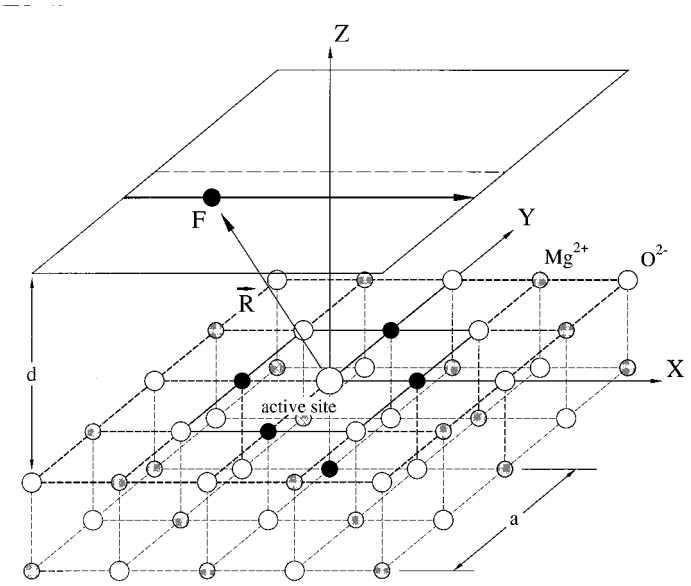

FIG. 2. Sketch of the F-MgO collision system. The cluster, comprising the active O^{2-} site (black) and the five nearest-neighbor Mg^{2+} sites (dark gray) is embedded in a—partly shown—grid of alternating point charges ($Q=\pm 2$), corresponding to Mg^{2+} (gray) and O^{2-} (white). The F projectile moves in the X direction parallel to the X-Y plane at a distance $Z=d$ from the surface. a is the lattice constant.

tion of model system and computational details, and Sec. IV presents the results of our calculations and a comparison with the available experimental data.

II. THEORY

Differing from the alkali-halide targets considered in Ref. [17], the lattice of MgO consists of doubly charged ions of alternating charge, $Q=\pm 2$ [37,38], of which the negative one, O^{2-}, does not exist as a stable free ion [39] and is a rather diffuse, highly polarizable object when embedded in the crystal structure.

At the same time, MgO is similar to the alkali halides in that it is a predominantly ionic crystal whose valence electrons are localized at the oxygen anion sites. MgO has a NaCl structure with a lattice constant of $a=7.9554$ a.u. [40–42], similar to that of LiF ($a=7.6$ a.u. [42]), for instance. Also, MgO shows nearly no surface reconstruction; along its most stable, nonpolar (100) surface the values for rumpling and relaxation are both smaller than 1% [41,43,44]. The band structure of MgO is similar to those of the alkali halides (Fig. 1), and the width of its band gap, $E_g \simeq 7.8$ eV [45,46], is comparable to the alkali halides as well. These similarities made it promising to address the theoretical description of the charge-transfer process with the method put forward in [17].

A. Binary encounter model

The basic premise of the binary encounter model is the following: During the interaction of the projectile with a given anion (''active site''), a hole can be created at the active site by transfer of one of its valence electrons to the projectile. It is assumed that on the time scale of the interaction between the projectile and the active site this hole cannot hop to other lattice sites. As in Ref. [17], we will treat the charge-transfer process between the projectile and the surface as an atom-atom-like collision of the neutral fluorine projectile, P, with a doubly charged oxygen ''active site'' of the lattice, A,

$$P^0 + A^{2-} \rightarrow P^- + A^-, \tag{1}$$

taking place in the presence of the field of the remaining lattice ions, considered as spectators.

The active O^{2-} site is placed at the origin of the target reference coordinate system, XYZ, as shown in Fig. 2. Appropriate for the treatment of the electron transfer process as a binary encounter, we will also use a rotating coordinate system, xyz, the z axis of which coincides with the molecular axis $\vec{R}$, while the y axis remains in the surface plane, and the x axis is perpendicular to both. The computations follow essentially the method reported in Ref. [17], so we will give only a brief outline in the following.

B. Role of the crystal potential

It is instructive to take a brief look at the behavior of the potential ''felt'' by the negatively charged projectile in the final state of the charge-transfer reaction [the right-hand side of Eq. (1)]. For simplicity we will consider the projectile and the ionic crystal (including the active site) in the point charge picture. A negatively charged projectile ($q=-1$) experiences a potential of

$$V_{\mathrm{Mad}}(\vec{R}) = \sum_{k(\vec{R}_k \neq 0)} \frac{qQ_k}{|\vec{R}-\vec{R}_k|} + \frac{1}{R}. \tag{2}$$

Here the sum runs with exception of the active site over all k lattice sites with charges Q_k of the (semi-)infinite crystal. The second term in the right-hand side of Eq. (2) takes into

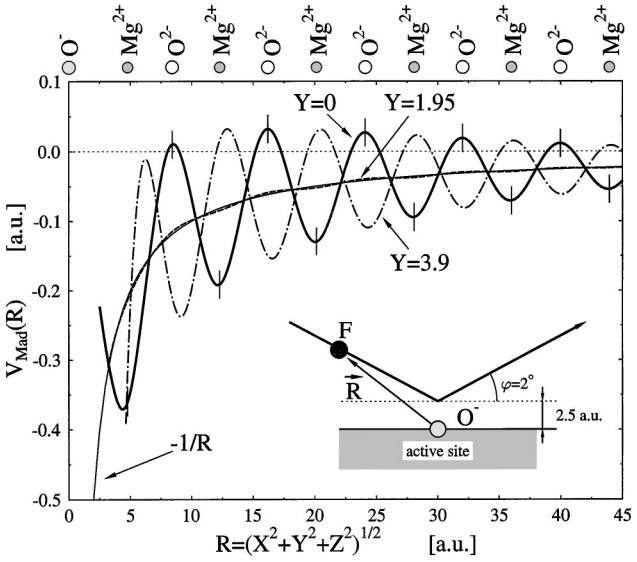

FIG. 3. Madelung potential V_{Mad}, for different impact parameters Y, *along* a grazing trajectory incident on a small MgO (100) cluster. The active row is drawn on top. V_{Mad} shows strong oscillations for trajectories above the alternating lattice charges. In between rows, this effect is reduced. Extrema, near the point of closest approach to the nth ion, $R_e(n)=\sqrt{\xi^2+z_0^2}\cos\varphi$ (with $\xi=na$), are offset slightly against the ion positions, $R_i(n)=\sqrt{\xi^2+(z_0+\xi\tan\varphi)^2}$, marked with thin vertical dashes. For comparison, there is also drawn the simple $-1/R$ potential due to the hole at the active site.

account the interaction between the projectile and the active O^{2-} site which is left with a charge of $Q=-1$ after removal of an electron. The presence of this so-called Madelung potential [47] is one of the salient differences between metal and alkali-halide targets. Adding $1/R-1/R$ to Eq. (2), it can be recast as

$$V_{\mathrm{Mad}}(\vec{R})=\sum_k \frac{qQ_k}{|\vec{R}-\vec{R}_k|}-\frac{1}{R}, \tag{3}$$

where the summation now runs over all lattice sites including the active site with charge -2. The first term in Eq. (3) gives thus the interaction of the external $q=-1$ charge with the unperturbed surface of the MgO crystal.

Since the crystal is neutral, the first term in Eq. (3) is small for moderate projectile-surface separations, and one can show that it falls off exponentially with increasing distance [19]. Therefore, the behavior of V_{Mad} is determined by the second, attractive, term. This term represents the interaction between the projectile and the hole left at the active site after removal of an electron, which can also be viewed as the creation of a $+1$ charge on the previously neutral surface [17].

Figure 3 shows as an example for grazing incidence ($\varphi=2°$) on the (100) surface of a small MgO cluster (modelled by ± 2 point charges) the behavior of V_{Mad} for three different impact parameters Y *along the trajectory*. As the trajectory passes the alternating lattice charges ($Q=\pm 2$) above the row of atoms containing the active oxygen site (''active row,'' $Y=0$) the potential shows strong oscillations with maxima (minima) close to the O^{2-} (Mg^{2+}) sites. It does not, however, saturate near the origin as seen for alkali-halide surfaces [17] because the negatively charged projectile after capture is repelled by the remaining negative charge on the active site (O^-).

For $Y=3.9\simeq a/2$ the trajectory passes the next row of atoms ($Q=\mp 2$), and we find essentially the same behavior, just with the opposite sign. As expected, for a trajectory in between two rows ($Y=1.95\simeq a/4$) the effect of the alternating lattice charges is nearly canceled, so that the Madelung potential closely follows the simple $-1/R$ Coulomb potential resulting from the hole located at the active site.

C. Dynamic charge evolution

The projectile-surface charge-transfer process basically involves a redistribution of an electron from one of the valence $2p$ orbitals of the active O^{2-} to one of the valence $2p$ orbitals of the projectile, and also an intra-atomic charge redistribution among the orbitals of the active site or the projectile during the interaction time.

The dynamics of the charge transfer is described by the time-dependent Schrödinger equation

$$i\frac{d}{dt}\Psi=\hat{H}\Psi, \tag{4}$$

where $\hat{H}$ is the electronic Hamiltonian. Owing to the closed shell structure of the F^- and O^{2-} ions, the electronic wave function Ψ can be expanded in a six state basis of $2p$-type diabatic [48] valence orbitals,

$$\Psi=\sum_{k=1}^{6} b_k\phi_k, \tag{5}$$

with

$$\phi=\{\phi^P_{p_x},\phi^P_{p_y},\phi^P_{p_z};\phi^A_{p_x},\phi^A_{p_y},\phi^A_{p_z}\}. \tag{6}$$

Here, the $\phi^P_{p_\mu}$ ($\mu=x,y,z$) correspond to the projectile state and the $\phi^A_{p_\mu}$ to the target state, with the hole occupying the p_μ orbital of the projectile ($P^0_{p_\mu}$) or of the active site ($A^-_{p_\mu}$). After insertion of Eq. (5) into Eq. (4) we arrive at

$$i\frac{d}{dt}\vec{B}=\{\mathcal{H}-i\mathcal{T}\}\vec{B}, \tag{7}$$

where $\vec{B}$ is the column vector of the coefficients b_k in Eq. (5). The off-diagonal elements h^μ of $\mathcal{H}$ (the matrix of the Hamiltonian in the diabatic basis representation) between $\phi^P_{p_\mu}$ and $\phi^A_{p_\mu}$ states induce electron transitions between the two collision partners and the remaining off-diagonal elements are related to polarization-type distortions [17]. The additional Coriolis coupling matrix $\mathcal{T}$ is introduced by the aforementioned choice of a rotating coordinate system following the projectile; for details, see Ref. [17].

The Hamiltonian matrix $\mathcal{H}$ needs to be known at each point along the collision trajectory. Based on the modeling of the system, presented in the following section, $\mathcal{H}$ can be

computed by means of standard quantum chemistry computer codes as described in Ref. [17] (we used the program HONDO [49]).

III. IMPLEMENTATION

A. Modeling of the system

In order to represent the electronic states associated with the—possibly negatively charged—fluorine projectile, we chose an expansion in terms of a double-ζ $(11s6p)/[5s3p]$ basis comprising 17 Gaussian-type orbital (GTO) basis functions (Ref. [50], Table 9.66.1). This basis was augmented by diffuse and polarization orbitals represented by three more GTO basis functions (one *s*, one *p*, and one *d* orbital). The exponents of these orbitals were $(\zeta_s^P, \zeta_p^P, \zeta_d^P) = (0.110\,38, 0.069, 0.8)$. The MgO(100) crystal surface was modeled by a three-dimensional grid of 784 atoms arranged in four parallel layers with a lattice constant *a* of 7.9554 a.u.

For the electrons on the active O^{2-} site, we used a contracted double-ζ oxygen $(11s6p)/[5s3p]$ basis set with 17 GTO basis functions (Ref. [50], Table 8.71.1). This basis was also augmented by three more GTO basis functions: one *s*, one *p*, and one *d* orbital with exponents $(\zeta_s^A, \zeta_p^A, \zeta_d^A) = (0.084\,56, 0.056\,53, 0.06)$ to account for the—compared with atomic oxygen—more diffuse electron cloud of O^{2-} and its large polarizability [51]. These features of O^{2-} result in a small probability density of its wave function in the vicinity of its five nearest-neighbor (NN) Mg^{2+} ions [43,52].

To achieve a proper representation of the active site wave functions throughout the whole unit cell, and, in particular, to take into account the orthogonality constraint with respect to the inner Mg^{2+} orbitals, we used a pseudopotential description of the Mg^{2+} ions on the five NN sites as suggested in Refs. [37,53–57]. The ten core electrons of the Mg^{2+} ions on the five NN sites were described by an ℓ-dependent effective core potential (ECP) [58]. To describe the Mg valence orbitals, we introduced at each NN Mg^{2+} site an additional basis set of six uncontracted GTOs compatible with the ECPs (Ref. [58], Tables 5 and 13).

This six-atom cluster such constructed was embedded in the grid of the remaining 778 lattice ions, taken to be point charges (PCs) of charge $Q = \pm 2$. These PCs establish the Madelung field (converged to better than 1.5×10^{-5} a.u.) in which the projectile interacts with the active site in the embedded cluster (Fig. 2). The use of $Q = \pm 2$ PCs to represent the ''nonactive'' sites of the ionic crystal has been shown to give correct results in quantum chemistry studies of various systems interacting with a MgO surface [54,55,57,59].

With this description of the crystal surface, for the O^{2-} $2p_\mu$ valence orbitals we obtain energy values of $E_{x,y} = -11.74$ eV and $E_z = -11.13$ eV, in close agreement with the value of -11.5 eV obtained from experimental [46] and theoretical [60] MgO(100) band-structure investigations. (Tests performed without the GTOs on the Mg^{2+} NN ions gave energies about 1.3 eV too close to the vacuum level.)

B. Computation of the static $\mathcal{H}$ matrix

For grazing incidence and small distances from the surface, the projectile moves *almost parallel* to it, so that during the binary encounter with the active site the projectile can be assumed to follow a trajectory which is piecewise parallel to the surface plane (see Figs. 2 and 4).

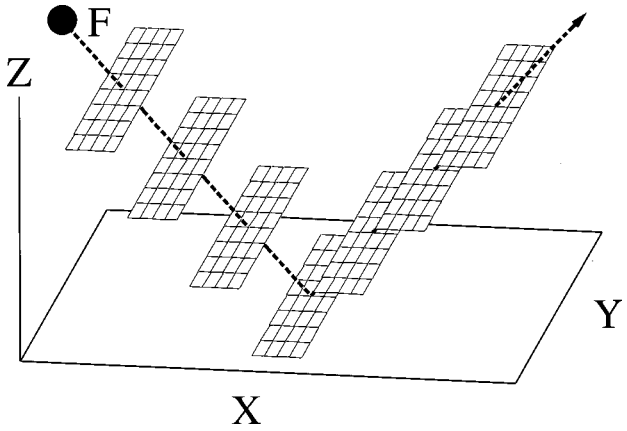

FIG. 4. Decomposition of the space above the crystal into layers parallel to the surface (sketch). Within these layers, the actual projectile trajectory is modeled by piecewise parallel, straight-line trajectories in the *X* direction.

The computation of the *static* $\mathcal{H}$ matrix in Eq. (7) was performed for a number of such trajectories at different altitudes *Z*. More specifically, $\mathcal{H}$ was calculated on a discrete three-dimensional (3D) grid for 46 410 points in front of the surface, using 70 points from 0–12.5 a.u. in the *X* direction, 51 points from 0–7.5 a.u. in the *Y* direction, and 13 points from 2.3–5.2 a.u. in the *Z* direction. The *X*-*Y* grid spacing was smaller close to the active site. The *Z* range was determined as follows: The distance of closest approach is given by the projectile energy (Sec. III C) while the largest distance considered here was characterized by the onset of nonzero electron transfer interactions ($h^\mu > 0$) in the considered velocity range. There were no significant contributions from layers outside this *Z* range, as tests for $Z = 5.5$ confirmed. For the *dynamic* charge-transfer calculations, we used a spline fit to the discrete $\mathcal{H}$ data, performed along the projectile trajectory, which in turn was determined as outlined in Sec. III C.

C. Trajectory

The projectile of mass m_P moves on a trajectory determined from the scattering potential by Newton's equation of motion. The effective scattering potential U_e experienced by the projectile is given by the sum

$$U_e(\vec{R}) = \sum_i V_{P,O^{2-}}(\vec{R} - \vec{R}_i) + \sum_j V_{P,Mg^{2+}}(\vec{R} - \vec{R}_j) \quad (8)$$

of the binary interaction potentials $V_{P,X}$ of the projectile with the O^{2-} and Mg^{2+} ions on the lattice sites. We have obtained these binary interaction potentials from the present Hartree-Fock (HF) calculations because it is known [61,62] that those obtained using the Thomas-Fermi-Moliere (TFM) or Ziegler-Biersack-Littmark (ZBL) screening functions [3,63] fail to reproduce experimental data for low-energy collisions. A lateral average in the *X*-*Y* plane over Eq. (8) (''continuum approximation'') leads to a *Z*-dependent scattering potential $U(Z)$, and is well justified for a grazing trajectory.

Along such a trajectory, the projectile with a velocity component $v_\perp$ perpendicular to the surface reaches its turn-

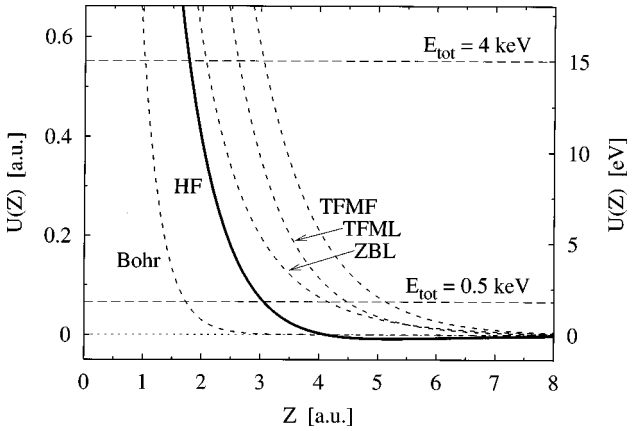

FIG. 5. Distance-dependent scattering potential $U(Z)$ in the continuum approximation. The solid line was obtained from our Hartree-Fock (HF) calculations. For comparison, drawn with dotted lines are the curves computed using the screening functions by Bohr, Ziegler-Biersack-Littmark (ZBL), and Thomas-Fermi-Moliere using either the Firsov (TFMF) or Lindhardt (TFML) screening lengths. The distance of closest approach of these models differs considerably in the projectile energy range $E_{\mathrm{tot}}=0.5-4$ keV.

ing point at the distance Z_{min} defined by

$$U(Z_{\mathrm{min}})=\tfrac{1}{2}m_P v_\perp^2. \tag{9}$$

Figure 5 shows the resulting averaged surface potential, from which a range for $Z_{\mathrm{min}}=1.8-3$ a.u. can be deduced for the projectile energies here considered. For comparison we also show the potentials obtained using the screening models by Bohr, ZBL, and TFM (for the latter using either the Firsov or Lindhardt screening length).

IV. RESULTS

A. Behavior of ΔE and h

The HF calculations allow to obtain the position-dependent diabatic energy differences $\Delta E^\mu(\vec{R})$ as well as the transfer-matrix elements $h^\mu(\vec{R})$. The diabatic energy difference ΔE^μ between the initial and final states corresponding, respectively, to the left- and right-hand sides of Eq. (1), is defined as

$$\Delta E^\mu(\vec{R})=E_{P^-+A^-_{p_\mu}}(\vec{R})-E_{P^0_{p_\mu}+A^{2-}}(\vec{R}). \tag{10}$$

This energy difference is a very important quantity which determines, together with h^μ, the efficiency of the charge-transfer process. Figures 6–8 show the diabatic energy differences and the electron transfer interactions of the x, y, and z orbitals for trajectories at large, medium, and low altitude Z, and different lateral displacements Y from the active row. The $Y=0$ trajectory is located right above this row, the one for $Y=3.90\simeq a/2$ lies almost above the next row, and the one for $Y=1.95\simeq a/4$ is roughly in the middle of the two. These figures clearly show the confluence of the energy levels discussed in detail in Ref. [17]. As illustrated in Sec. II B, this energy-level confluence is already present in the simple PC model. (The X range used for Figs. 6–8 corresponds to the first few oscillations seen in Fig. 3.)

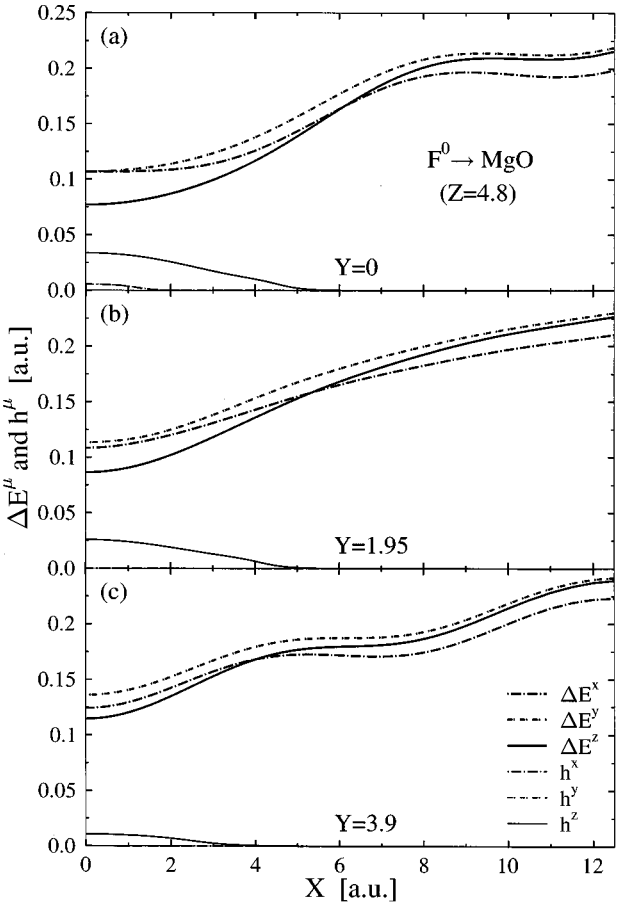

FIG. 6. Diabatic energy difference ΔE^μ (upper curves at $x=12$) and electron transfer interaction h^μ for the x, y, and z orbitals at large altitude $Z=4.8$ a.u. and different impact parameters Y.

Figure 6 shows the diabatic energy differences and the electron transfer interactions for an altitude of $Z=4.8$ a.u. Here the strongest energy-level confluence and the largest electron transfer interaction can be seen for motion along the active row [Fig. 6(a)]. The features of the curves are readily explained from the geometry of the problem: When the projectile is located above the active site ($X=Y=0$), the x and y orbitals lie in a plane parallel to the surface and, thus, are energetically degenerate. Close to the active site the z orbitals show the smallest energy difference and the largest transfer interaction due to the orientation of the projectile z lobe, pointing toward the surface along the molecular axis between active site and projectile. For increasing values of X, the energy difference of the z orbitals begins to approach that of the slowly changing y orbitals, at some point crossing the curve for the x orbitals. The curve for the x orbitals assumes the lowest value for larger values of X since *asymptotically* the projectile x lobe is pointing towards the surface while the z lobe is parallel to it. For increasing lateral distance from the active row [Figs. 6(b) and 6(c)] the level confluence and the transfer interaction are reduced further. In general, the energy differences are too large and the electron transfer interactions too small at large altitudes to allow efficient electronic transitions.

Figure 7 shows the energy differences and electron trans-

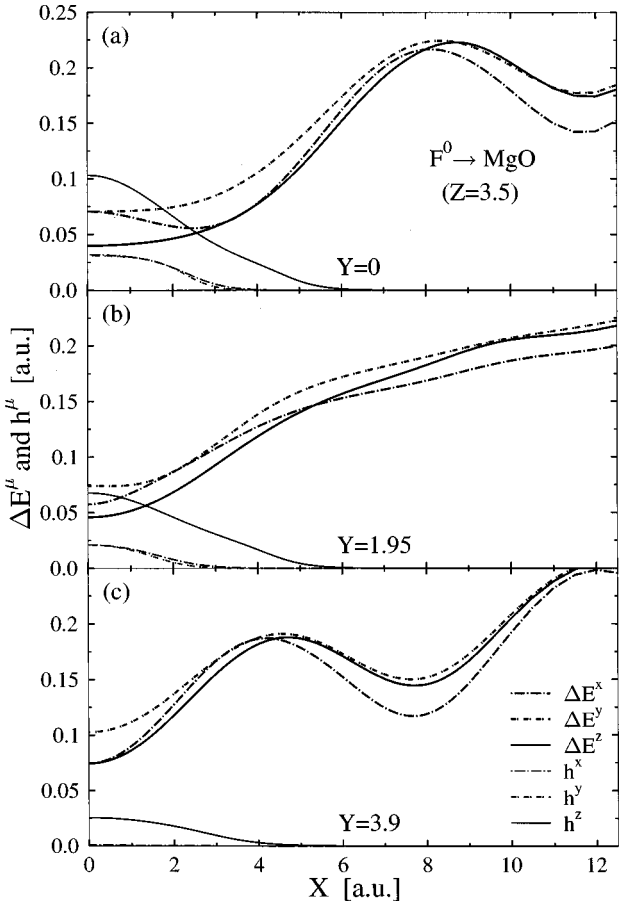

FIG. 7. Like Fig. 6, but at medium altitude, $Z=3.5$ a.u.

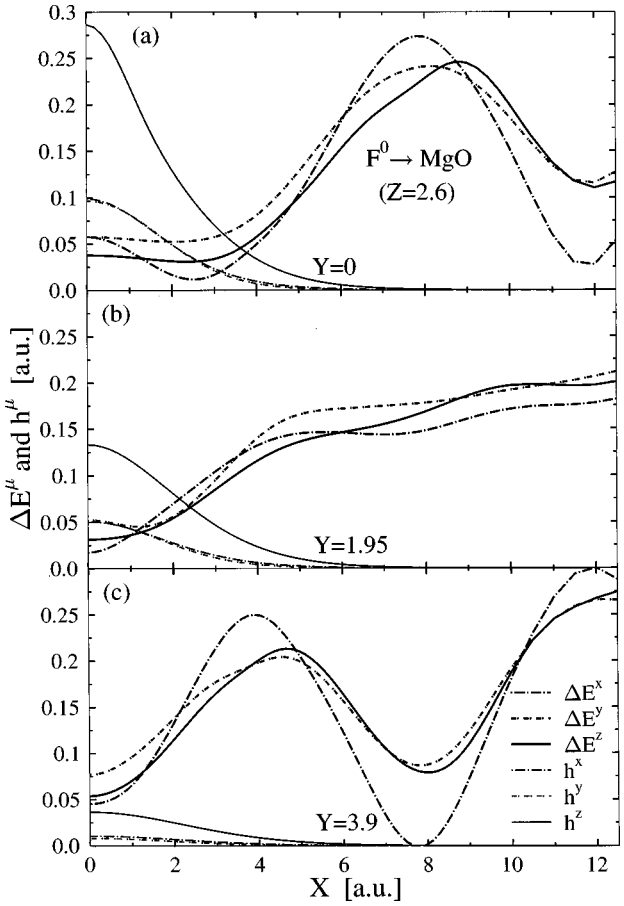

FIG. 8. Like Fig. 6, but at small altitude, $Z=2.6$ a.u.

fer interaction data for $Z=3.5$ a.u. The z orbitals show again the largest transfer interaction and initially the strongest energy-level confluence. For $X\simeq 3.5-3.9(\simeq d)$, the x and z lobes of the projectile straddle the Mg^{2+} ion on the NN site in the active row nearly symmetrically, such that they have nearly the same distance from the surface, and their energies coincide. For larger values of X the energy level difference of the x orbitals becomes the smallest, as outlined above. For $Y=3.9(\simeq a/2)$ we encounter the same situation at $X=0$: for obvious symmetry reasons, the positions $(0,a/2)$ and $(a/2,0)$ are energetically equivalent, and the x and z energy-level differences coincide. The onset of a contribution from the x and y orbitals can be expected at least in the vicinity of the active row (small impact parameters Y). Due to the reduced energy differences and increased electron transfer interactions one can expect more efficient electronic transitions than for the case shown in Fig. 6.

For the smallest distance shown, $Z=2.6$, finally, the system exhibits also the smallest energy differences ΔE^μ and the largest electron transfer interactions (Fig. 8). Here efficient Demkov-type charge transfer between quasiparallel energy terms [64,65] will take place. Smaller altitudes are not accessible to the projectile within the energy range considered here.

In order to illustrate the dependence of energy-level difference and electron transfer interaction on the periodic crystal structure, we show a three-dimensional plot of these quantities at $Z=5.2$ a.u. [Fig. 9(a)] and $Z=2.6$ a.u. [Fig. 9(b)] for the z orbitals, for which the effect is most pronounced. For high altitudes [Fig. 9(a)] the effect of the Madelung field is smoothed out, ΔE^z varies slowly, and the electron transfer interaction h^z is very small. For small distances [Fig. 9(b)], on the other hand, the electron transfer interaction becomes large and the periodic lattice structure leaves a clear signature in ΔE^z. From the behavior of ΔE^z and h^z one can expect that the electron transfer should, indeed, be localized near the active site.

B. Polarization effects

Upon electron capture, the projectile (now P^-) carries a charge of -1. Moreover, the hole left behind at the active site is equivalent to a charge of $+1$, created at the surface of the previously neutral crystal. The resulting electric dipole moment $e\vec{R}$ creates a field which polarizes the lattice ions (up to here considered mere point charges), thus introducing additional field-induced dipole contributions to the total energy of the system. The corresponding correction term (''Mott-Littleton interaction'' [28,66]) enters the energy of the system in the final (P^-+A^-) state, and is given by

$$E_{\mathrm{ML}}(\vec{R})=-\frac{1}{2}\sum_k \alpha_k\left(\frac{\vec{R}_k}{R_k^3}-\frac{\vec{R}_k-\vec{R}}{|\vec{R}_k-\vec{R}|^3}\right)^2, \qquad (11)$$

where k runs over all lattice sites $\vec{R}_k$ except the active one, and the polarizabilities α_k of the lattice ions ($\alpha_{Mg^{2+}}=0.644a_0^3$, $\alpha_{O^{2-}}=11.116a_0^3$) are taken from Ref. [51]. The

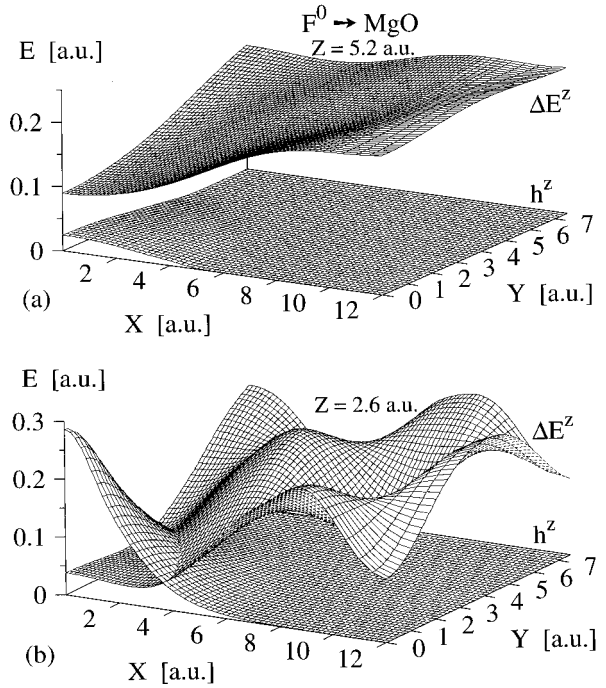

FIG. 9. 3D plots of the energy difference ΔE^z and electron transfer interaction h^z. At high altitude (a), the effect of the Madelung field is smoothed out and the magnitudes of ΔE^z and h^z differ. At low altitude (b), ΔE^z and h^z are of comparable size close to the active site (origin), facilitating Demkov-type transitions.

correction introduced by Eq. (11) leads to a reduction of $\Delta E(\vec{R})$ by about 0.0125 a.u. near the active site, and it can be expected to facilitate the charge-transfer process. We have performed the final charge-transfer calculations with and without inclusion of this correction in order to assess its influence on the negative-ion production.

C. Capture probabilities

With the ingredients discussed in the preceeding sections, we can solve the time-dependent equation (7) numerically along a number of straight line trajectories $\vec{R}(t) = (vt, Y, Z)$, averaging over the results obtained with three sets of initial conditions $\vec{B}^j(t \to -\infty) = \{\delta_{kj}\}$ with $k = 1-6$, where $j = 1$, 2, and 3 correspond to the hole initially occupying the p_x, p_y, or p_z orbital of the projectile.

Figure 10 shows an example of the electron-capture probability per active site, $P_{\text{site}}(v_\parallel, Y, Z)$, as a function of the parallel velocity $v_\parallel$ and the displacement Y from the active row (''impact parameter'') for a medium altitude ($Z = 3.5$ a.u.). The features seen in the low-velocity, low-impact-parameter, region can be related to Stueckelberg oscillations [67] known from atomic collision physics. The integrated capture probability (averaged over the impact parameter)

$$P(v_\parallel, Z) = \frac{2}{a} \int_0^{a/2} P_{\text{site}}(v_\parallel, Y, Z)\, dY \qquad (12)$$

for this altitude is shown in Fig. 11 with a solid line. It displays a sharp low-velocity threshold. The dashed line in

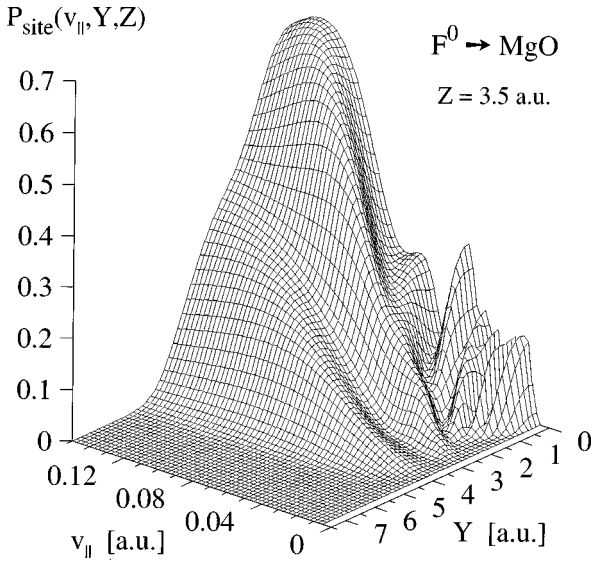

FIG. 10. Electron-capture probability per active site, $P_{\text{site}}(v_\parallel, Y, Z)$, as a function of parallel velocity $v_\parallel$ and impact parameter Y at medium altitude ($Z = 3.5$ a.u.).

Fig. 11 shows the integrated capture probability obtained from our calculations without inclusion of the Mott-Littleton (ML) interaction. As discussed above, the additional ML correction reduces the energy defect ΔE of the charge-transfer reaction, and therefore increases the electron-capture probability. The absolute value of this reduction near the active site may seem moderate, yet its size *relative* to the magnitude of ΔE^μ in this region makes it significant. We should note that the velocity dependence of the capture probability per site can be related to the Demkov-Nikitin model [64,65] for near-resonant electron transitions (see the discussion in Ref. [17]).

Figure 12 shows the integrated probabilities $P(v_\parallel, Z)$ as a function of projectile altitude ($2.3 \leqslant Z \leqslant 5.2$) and velocity (shown is the case without the ML correction). It can be seen that the low-velocity range contributes only for small and intermediate distances to the negative-ion production, while

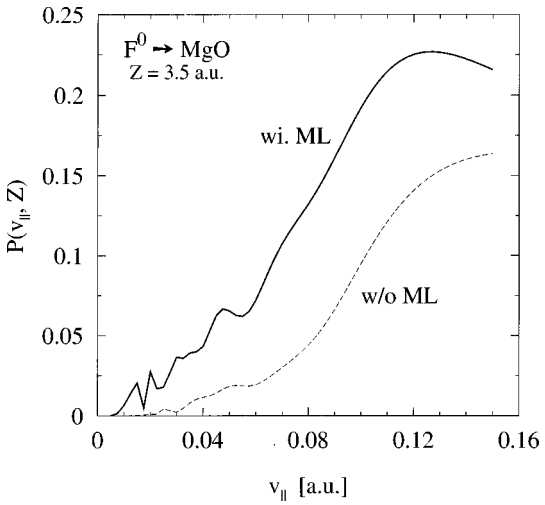

FIG. 11. Integrated electron-capture probability $P(v_\parallel, Z)$ for $Z = 3.5$ a.u., obtained with (solid line) and without (dashed line) inclusion of the Mott-Littleton (ML) interaction.

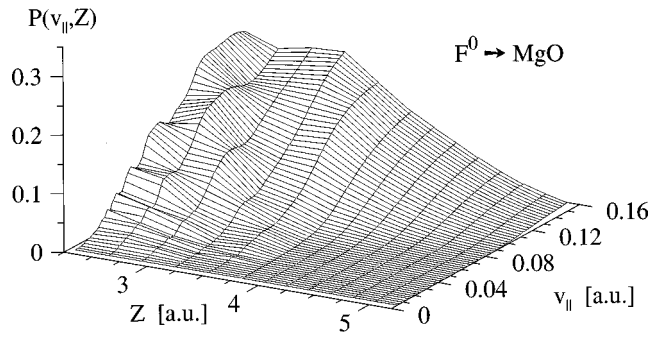

FIG. 12. Integrated capture probability $P(v_\parallel, Z)$ as a function of projectile altitude Z and velocity $v_\parallel$. (Shown is the case without inclusion of the Mott-Littleton contribution.)

high altitudes make no relevant contribution even for larger velocities. The latter observation lends additional support for the range of altitudes chosen for our calculations (cf. Sec. III B).

From these altitude-dependent capture probabilities we can now calculate the total negative ion formation probabilities along the actual trajectory $Z(X(t))$ [cf. Fig. 4] for a grazing incidence collision from

$$P_{\mathrm{tot}}(v_\parallel) = 1 - \prod_{i=1}^{N} \{1 - P_i(v_\parallel, Z_i)\}, \tag{13}$$

where the number of collisions, N, also depends on the trajectory, and $Z_i = Z(X(t_i))$ is the altitude of the projectile during the ith collision.

A comparison of the results obtained under omission and inclusion of the ML interaction, respectively, with the experimental data [36] for negative-ion production from neutral projectiles (solid circles) is given in Fig. 13.

The applicability of the binary encounter model [17] to the considered F-MgO collision system is confirmed by the two theoretical curves, which bracket the low-velocity part of the experimental data and reproduce the velocity threshold for negative-ion production. These results also illustrate the sensitivity of the negative-ion production to rather small

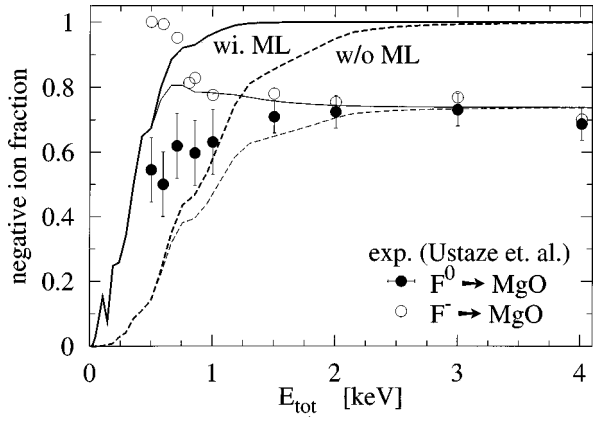

FIG. 13. Total negative-ion fraction, obtained with (thick solid line) and without (thick dashed line) inclusion of the Mott-Littleton (ML) interaction in comparison with the experimental data by S. Ustaze *et al.* [35]. The thin lines show the total negative-ion fraction after multiplication with a fit to the experimental loss data.

changes in the energy difference (the reduction of ΔE due to the ML term is of the order of 0.5 eV in the interaction region). In view of the extreme sensitivity of the theoretical results to the energy difference ΔE, we find the agreement between theory and experiment in the low-velocity range quite satisfactory.

It is, indeed, rather difficult to calculate the different components entering ΔE (for instance, the position of the valence band) with a precision of a fraction of an eV. Our computation makes use of Koopmans' theorem [68], which is known to overestimate the electron affinites. This energy defect has been corrected for the fluorine projectile, where the HF electron affinity was $\simeq 0.054$ a.u. stronger than the experimental value. For the second electron affinity of the active oxygen site such a correction could not be performed, and we had to rely on the good agreement of the energy range of the $O^{2-}\,2p_\mu$ valence orbitals with available band-structure data (see Sec. III A).

In addition, let us note that for the charged projectile the actual incidence and exit angles close to the surface differ from the asymptotic values measured experimentally. This deviation is caused by the image charge interaction between the projectile and the surface [8,69]. The turning point of the trajectory cannot be exactly determined due to these uncertainties in the determination of the projectile velocity component normal to the surface at small separations. This may account for part of the discrepancies between our theoretical results and the experimental data. As in Ref. [17], the computations were performed using an *effective* grazing angle β, determined from the relation

$$E_{\mathrm{tot}}\beta^2 = E_{\mathrm{tot}}\varphi^2 + \eta, \tag{14}$$

where E_{tot} is the energy of the beam in eV, and $\eta = 0.6$ eV accounts for the image charge attraction toward the surface. However, tests performed for values of η from 0 to 2.5 eV showed that for the present collision system this effect is small compared to that of the ML interaction.

The experimental data reported in Ref. [36] for *negatively charged* projectiles (open circles in Fig. 13) document the existence of an electron loss channel. At low projectile energies, the electron loss rate is small, and the negative-ion fraction obtained with negative projectiles reaches 100%. This observation supports the validity of the low-energy part of the present calculation, performed ignoring electron loss. With increasing projectile energy, both capture and loss rates increase, and the initial charge-state dependence of the measured negative ion fraction decreases. Its value corresponds to the equilibrium population determined by the competition between electron capture and loss near the surface. For the collision system at hand, the experimental negative-ion fraction stabilizes, independent of the initial projectile charge, at about 70%. This is a feature which our theoretical results do not reproduce because electron-loss effects are not included in the present model.

Such loss effects could be caused, for instance, by kinematic resonance with the valence band or by the Okorokov effect [70] (''stripping off'' of an electron in the periodic potential of the crystal surface; see Fig. 3). They are not included in the present model but are a subject of our current research. The thin lines in Fig. 13 show, as a rough estimate,

the total negative-ion fraction obtained after a multiplication of our theoretical results with a fit to the experimental *loss* data (open circles in Fig. 13).

V. CONCLUSIONS

The theoretical results presented in this paper for the negative-ion production from fluorine projectiles during slow, grazing-incidence, collisions with a MgO(100) surface show that the binary encounter model for the description of charge-transfer processes on ionic crystal surfaces [17] can also be applied to explain the negative-ion production observed [36] during collisions with insulating oxide surfaces.

The theoretical results obtained from this model provide a good description of the experimental data. The two theoretical curves (with and without inclusion of lattice polarization effects) bracket the available experimental data [36], and reproduce the proper low-velocity behavior. Loss effects, which seem to become influential at larger velocities and lead to a saturation of the experimental negative ion yield, are presently not included in the model. Hence, further development of the theoretical approach is needed in order to describe the complete velocity range of the experimental results [36].

ACKNOWLEDGMENTS

We would like to thank V. A. Esaulov, L. Guillemont, and S. Ustaze for stimulating discussions during the course of these calculations. This work was supported by the European Union under Contract No. ERBFMBICT971983.

[1] R. Brako and D. M. Newns, Rep. Prog. Phys. **52**, 655 (1989).
[2] J. Los and J. J. C. Geerlings, Phys. Rep. **190**, 133 (1990).
[3] J. Burgdörfer, in *Review of Fundamental Processes and Applications of Atoms and Ions*, edited by C. D. Lin (World Scientific, Singapore, 1993), p. 517.
[4] H. Shao, D. C. Langreth, and P. Nordlander, in *Low Energy Ion-Surface Interactions*, edited by J. W. Rabalais (Wiley, New York, 1994), p. 118; B. H. Cooper and E. R. Behringer, in *ibid.* p. 264.
[5] P. Varga and U. Diebold, in *Low Energy Ion-Surface Interactions* (Ref. [4]), p. 355.
[6] V. E. Henrich, G. Dresselhaus, and H. J. Zeiger, Phys. Rev. B **22**, 4764 (1980).
[7] R. Souda, W. Hayami, T. Aizawa, and Y. Ishizawa, Phys. Rev. B **50**, 1934 (1994).
[8] C. Auth, T. Hecht, T. Igel, and H. Winter, Phys. Rev. Lett. **74**, 5244 (1995).
[9] T. Neidhart, F. Pichler, F. Aumayr, H. P. Winter, M. Schmid, and P. Varga, Phys. Rev. Lett. **74**, 5280 (1995).
[10] J. Limburg, S. Schippers, R. Hoekstra, R. Morgenstern, H. Kurtz, F. Aumayr, and H. P. Winter, Phys. Rev. Lett. **75**, 217 (1995).
[11] C. Auth, A. G. Borisov, and H. Winter, Phys. Rev. Lett. **75**, 2292 (1995).
[12] R. Souda, K. Yamamoto, W. Hayami, B. Tilley, T. Aizawa, and Y. Ishizawa, Surf. Sci. **324**, L349 (1995).
[13] C. Auth, *Wechselwirkung von Atomen und Ionen mit Metall- und Isolatoroberflächen bei streifender Streuung* (Shaker Verlag, Aachen, 1996).
[14] H. Winter, A. Mertens, C. Auth, and A. Borisov, Phys. Rev. A **54**, 2486 (1996).
[15] L. Liu, V. E. Henrich, W. P. Ellis, and I. Shindo, Phys. Rev. B **54**, 2236 (1996).
[16] J.-P. Briand, S. Thuriez, G. Giardino, G. Borsoni, M. Froment, M. Eddrief, and C. Sébenne, Phys. Rev. Lett. **77**, 1452 (1996).
[17] A. G. Borisov, V. Sidis, and H. Winter, Phys. Rev. Lett. **77**, 1893 (1996); A. G. Borisov and V. Sidis, Phys. Rev. B **56**, 10 628 (1997).
[18] L. Hägg, C. O. Reinhold, and J. Burgdörfer, Phys. Rev. A **55**, 2097 (1997).
[19] C. Auth, A. Mertens, H. Winter, A. G. Borisov, and F. J. García de Abajo, Phys. Rev. Lett. **79**, 4477 (1997).
[20] P. Stracke, F. Wiegershaus, S. Krischok, H. Muller, and V. Kempte, Nucl. Instrum. Methods Phys. Res. B **125**, 63 (1997).
[21] S. Kohiki, S. Fukushima, H. Yoshikawa, and M. Arai, Jpn. J. Appl. Phys. **36**, 2856 (1997); **37**, 2078(E) (1998).
[22] J. J. Ducrée, F. Casali, and U. Thumm, Phys. Rev. A **57**, 338 (1998).
[23] C. Auth, A. Mertens, H. Winter, A. G. Borisov, and V. Sidis, Phys. Rev. A **57**, 351 (1998).
[24] N. D. Lang and W. Kohn, Phys. Rev. B **1**, 4555 (1970).
[25] N. F. Mott, Trans. Faraday Soc. **34**, 500 (1938).
[26] P. H. Citrin and T. D. Thomas, J. Chem. Phys. **57**, 4446 (1972).
[27] M. Piacentini, Solid State Commun. **17**, 697 (1975).
[28] G. D. Mahan, Phys. Rev. B **21**, 4791 (1980).
[29] A. B. Kunz, Phys. Rev. B **26**, 2056 (1982).
[30] D. Heskett, K.-H. Frank, K. Horn, E. E. Koch, H.-J. Freud, A. Baddorf, K.-D. Tsuei, and E. W. Plummer, Phys. Rev. B **37**, 10 387 (1988).
[31] G. K. Wertheim, J. E. Rowe, D. N. E. Buchanan, and P. H. Citrin, Phys. Rev. B **51**, 13 675 (1995).
[32] *CRC Handbook of Chemistry and Physics*, 77th ed., edited by D. R. Linde (CRC Press, Boca Raton, FL, 1997).
[33] G. A. Somorjai, *Chemistry in Two Dimensions: Surfaces*. (Cornell University Press, Ithaca, NY, 1981); G. A. Somorjai, *Introduction to Surface Chemistry and Catalysis* (Wiley, New York, 1994).
[34] V. E. Henrich and P. A. Cox, *The Surface Science of Metal Oxides* (Cambridge University Press, New York, 1996).
[35] M. Maazouz, L. Guillemot, S. Lacombe, and V. A. Esaulov, Phys. Rev. Lett. **77**, 4265 (1996).
[36] S. Ustaze, R. Verucchi, S. Lacombe, L. Guillemont, and V. A. Esaulov, Phys. Rev. Lett. **79**, 3526 (1997).
[37] F. Illas, A. Lorda, J. Rubio, J. B. Torrance, and P. S. Bagus, J. Chem. Phys. **99**, 389 (1993).
[38] C. Sousa, F. Illas, C. Bo, and J. M. Poblet, Chem. Phys. Lett. **215**, 97 (1993).
[39] Strictly, free O^{2-} has been observed at a pressure of 4

$\times 10^{-6}$ Torr, where it is estimated to have a life time of $10^{-7}-10^{-6}$ s [71].
[40] J. E. Mayer and M. M. Maltbie, Z. Phys. **75**, 748 (1932).
[41] J. B. Zhou, H. C. Lou, T. Gustafsson, and P. Häberle, Surf. Sci. **302**, 350 (1994).
[42] C. Kittel, *Introduction to Solid State Physics*, 7th ed. (Wiley, New York, 1996).
[43] Y. Li, D. C. Langreth, and M. R. Pederson, Phys. Rev. B **55**, 16 456 (1997).
[44] O. Robach, G. Renaud, and A. Barbier, Surf. Sci. **401**, 227 (1998).
[45] M. W. Williams and E. T. Arakawa, J. Appl. Phys. **38**, 5272 (1967); D. M. Roessler and W. C. Walker, Phys. Rev. **159**, 733 (1967); J. Opt. Soc. Am. **57**, 833 (1967).
[46] L. H. Tjeng, A. R. Vos, and G. A. Sawatzky, Surf. Sci. **234**, 269 (1990).
[47] E. Madelung, Phys. Z. **20**, 494 (1919).
[48] V. Sidis, Adv. Chem. Phys. **82**, 73 (1992).
[49] M. Dupuis, J. D. Watts, H. O. Villar, and G. J. B. Hurst, Comput. Phys. Commun. **52**, 415 (1989).
[50] R. Poirier, R. Kari, and I. G. Csizmadia, *Handbook of Gaussian Basis Sets* (Elsevier, New York, 1985).
[51] J. R. Tessman, A. H. Kahn, and W. Shockley, Phys. Rev. **92**, 890 (1953).
[52] U. Birkenheuer, J. C. Boettger, and N. Rösch, J. Chem. Phys. **100**, 6826 (1994).
[53] C. Satoko, M. Tsukada, and H. Adach, J. Phys. Soc. Jpn. **45**, 1333 (1978).
[54] G. Pacchioni and T. Minerva, Surf. Sci. **275**, 450 (1992).
[55] K. M. Neyman and N. Rösch, Chem. Phys. **168**, 267 (1992).
[56] M. A. Nygren, L. G. M. Pettersson, Z. Barandiarán, and L. Seijo, J. Chem. Phys. **100**, 2010 (1994).
[57] J. A. Mejías, A. M. Márquez, J. F. Sanz, M. Fernańdéz-García, J. M. Ricart, C. Sousa, and F. Illa, Surf. Sci. **327**, 59 (1995).
[58] W. R. Wadt and P. J. Hay, J. Chem. Phys. **82**, 284 (1985).
[59] J. M. Zuo, M. O'Keeffe, P. Rez, and J. C. H. Spence, Phys. Rev. Lett. **78**, 4777 (1997).
[60] S. Russo and C. Noguera, Surf. Sci. **262**, 245 (1992).
[61] A. D. Tenner, K. T. Gillen, T. C. M. Horn, J. Los, and A. W. Kleyn, Phys. Rev. Lett. **52**, 2183 (1984).
[62] D. M. Goodstein, R. L. McEachern, and B. H. Cooper, Phys. Rev. B **39**, 13 129 (1989).
[63] J. F. Ziegler, J. P. Biersack, and U. Littmark, *The Stopping and Range of Ions in Matter* (Pergamon, New York, 1985).
[64] Yu. N. Demkov, Zh. Eksp. Teor. Fiz. **45**, 195 (1963) [Sov. Phys. JETP **18**, 138 (1964)].
[65] E. E. Nikitin and S. Y. Umanski, *Theory of Slow Atomic Collisions* (Springer-Verlag, Berlin, 1984).
[66] N. F. Mott and M. J. Littleton, Trans. Faraday Soc. **34**, 485 (1938).
[67] E. C. G. Stueckelberg, Helv. Phys. Acta **5**, 369 (1932).
[68] T. Koopmans, Physica (Amsterdam) **1**, 104 (1934).
[69] H. Winter, J. Phys. C **8**, 10 149 (1996).
[70] V. V. Okorokov, Pis'ma Zh. Eksp. Teor Fiz. **2**, 175 (1965) [Sov. Phys. JETP **2**, 111 (1965)].
[71] Sir H. Massey, *Negative Ions: Autodetaching States of Specific Atomic Ions*, 3rd ed. (Cambridge University Press, Cambridge, 1976), p. 155.